

# Global Crustal Thickness Revealed by Surface Waves Orbiting Mars

D. Kim<sup>1</sup>, C. Duran<sup>1</sup>, D. Giardini<sup>1</sup>, A-C. Plesa<sup>2</sup>, S. C. Stähler<sup>1,3</sup>, C. Boehm<sup>1</sup>,  
V. Lekić<sup>4</sup>, S. M. McLennan<sup>5</sup>, S. Ceylan<sup>1</sup>, J. F. Clinton<sup>6</sup>, P. Davis<sup>7</sup>, A. Khan<sup>8</sup>,  
B. Knapmeyer-Endrun<sup>9</sup>, M. P. Panning<sup>10</sup>, M. Wiczorek<sup>11</sup>, P. Lognonné<sup>11</sup>

<sup>1</sup>Institute of Geophysics, ETH Zurich, Switzerland

<sup>2</sup>DLR, Institute of Planetary Research, Berlin, Germany

<sup>3</sup>Physik-Institut, Universität Zürich, Zurich, Switzerland

<sup>4</sup>Department of Geology, University of Maryland, College Park, USA

<sup>5</sup>Department of Geosciences, Stony Brook University, Stony Brook, USA

<sup>6</sup>Swiss Seismological Service, ETH Zurich, Zurich, Switzerland

<sup>7</sup>Department of Earth, Planetary, and Space Sciences, University of California Los Angeles, USA

<sup>8</sup>Institute of Geochemistry and Petrology, ETH Zurich, Zurich, Switzerland

<sup>9</sup>Bergisch Observatory, University of Cologne, Bergisch Gladbach, Germany

<sup>10</sup>Jet Propulsion Laboratory, California Institute of Technology, USA

<sup>11</sup>Université Paris Cité, Institut de physique du globe de Paris, CNRS, Paris, France

## Key Points:

- We present the first observation of Rayleigh waves that orbit around Mars up to three times.
- Group velocity measurements and 3-D simulations constrain the average crustal and uppermost mantle velocities along the propagation path
- The global average crustal thickness is 42-56 km and requires a large enrichment of heat-producing elements to explain local melt zones

---

Corresponding author: D. Kim, [doyeon.kim@erdw.ethz.ch](mailto:doyeon.kim@erdw.ethz.ch)

**Abstract**

We report observations of Rayleigh waves that orbit around Mars up to three times following the S1222a marsquake. Averaging these signals, we find the largest amplitude signals at 30 s and 85 s central period, propagating with distinctly different group velocities of 2.9 km/s and 3.8 km/s, respectively. The group velocities constraining the average crustal thickness beneath the great circle path rule out the majority of previous crustal models of Mars that have a  $>200$  kg/m<sup>3</sup> density contrast across the dichotomy. We find that the thickness of the martian crust is 42-56 km on average, and thus thicker than the crusts of the Earth and Moon. Together with thermal evolution models, a thick martian crust suggests that the crust must contain 50-70% of the total heat production to explain present-day local melt zones in the interior of Mars.

**Plain Language Summary**

The NASA InSight mission and its seismometer installed on the surface of Mars is now retired after  $\sim 4$  years of operation. We observe clear seismic signals from surface waves called Rayleigh waves that orbit around Mars up to three times from the largest marsquake recording during the mission. By measuring the wavespeeds at which those surface waves travel in different frequencies, we obtain the first seismic evidence that constrains the average crustal and uppermost mantle structures beneath the traveling path on a planetary scale. Using the new seismic observations together with indirectly measured gravity data, we confirm the findings from our previous analyses of surface waves that the density of the crust in the northern lowlands and the southern highlands is similar or different by no more than 200 kg/m<sup>3</sup>. Furthermore, we find the global average crustal thickness on Mars would be 42-56 km, much thicker than the Earth's and Moon's crusts. By exploring the thermal evolution of Mars, a thick martian crust requires about 50-70% of the heat-producing elements such as thorium, uranium, and potassium to be concentrated in the crust in order to explain local regions in the Martian mantle that can still undergo melting at present day.

**1 Introduction**

After more than 4 Earth years ( $\sim 1450$  sols) of operations on the martian surface monitoring the planet's ground vibrations, the InSight mission (Banerdt et al., 2020) is now retired which leads to the end of its seismometer (SEIS; Lognonné et al., 2019) operation. Throughout the mission, analyses of body waves from marsquakes (Giardini et al., 2020; InSight Marsquake Service, 2022; Ceylan et al., 2022) and impacts (Garcia et al., 2022; Posiolova et al., 2022) have led to important discoveries about the planet's crust (Lognonné et al., 2020; Knapmeyer-Endrun et al., 2021; Kim, Lekić, et al., 2021), mantle (Khan et al., 2021; Durán et al., 2022; Drilleau et al., 2022), and core (Stähler et al., 2021; Khan et al., 2022; Irving et al., 2022). Recent detection of fundamental mode surface waves and overtones, together with gravimetric modeling enabled the characterization of crustal structure variations away from the InSight landing site and showed that average crustal velocity and density structure is similar between the northern lowlands and the southern highlands (Kim, Banerdt, et al., 2022; Kim, Stähler, et al., 2022).

Earlier in the mission, the InSight science team produced 1-D models of Mars' interior (KKS21; named after the three publications of Knapmeyer-Endrun et al., 2021; Khan et al., 2021; Stähler et al., 2021) by inverting travel times of the body wave arrivals together with geophysical and geodynamical parameters as a function of composition, temperature, and pressure at depth. Recently, cosmochemical constraints on the nature of the mantle (e.g., Khan et al., 2022) have been used to construct a unified description of the planetary structure that can explain both observed geophysical measurements as well as the major element distribution. Using an expanded body wave dataset and the

73 new mantle composition of Mars, updated 1-D interior models of the planet are now avail-  
74 able (e.g., Durán et al., 2022).

75 Despite different approaches and the new compositional constraints incorporated  
76 into the modeling, more than 75% of the seismic body wave measurements are predom-  
77 inantly sensitive to the lithospheric structure between the Elysium Planitia and the Cer-  
78 berus Fossae where most of the planet’s seismicity (Stähler et al., 2022) and small me-  
79 teorite impacts have been observed (Garcia et al., 2022). Similarly, in those 1-D mod-  
80 els, crustal structure directly beneath the landing site of InSight is assumed to be rep-  
81 resentative of average martian crust. These observational limitations and modeling choices  
82 can significantly bias our inferences of the global interior structure and dynamics of Mars.

83 In this study, we identify Rayleigh waves that orbit around Mars up to three full  
84 cycles (up to R7; Fig. 1A) and report their group velocity measurements for S1222a, the  
85 largest seismic event recorded by InSight. With long- (LP) and very-long-period (VLP)  
86 analysis of the R2-R7 and three-dimensional (3-D) wavefield simulations, we obtain seis-  
87 mic wavespeeds in average crustal and mantle structures and improve previously reported  
88 estimates on global crustal thickness on Mars. We highlight the implications of the new  
89 constraints from our analysis for the planet’s interior structure and thermal evolution.

## 90 2 Data and Methods

91 The largest seismic event detected during the InSight mission is the  $M_W^{ma}$  4.7 marsquake  
92 S1222a (Kawamura et al., 2022) (Fig. 1B). The seismic waveforms of S1222a contain both  
93 minor-arc Rayleigh and Love waves (e.g., Beghein et al., 2022), overtones (Kim, Stähler,  
94 et al., 2022), and Rayleigh waves that propagate around Mars for one cycle (R2 and R3)  
95 (e.g., Panning et al., 2023). To extend our analysis and search for Rayleigh waves trav-  
96 eling multiple times around Mars, we consider a 10-hour long seismic recording of S1222a  
97 (InSight Marsquake Service, 2023)(Fig. S1). We apply marsquake seismic data process-  
98 ing techniques to remove electro-mechanical noise by the sensor and the lander (Scholz  
99 et al., 2020), to suppress spurious signals and to avoid misinterpretation of the SEIS data  
100 (Kim, Davis, et al., 2021). We restrict our analysis to the 25 to 100 s period range be-  
101 cause seismic energy observed outside this frequency range can be affected by atmospheric  
102 turbulence at various scales at longer periods (Banfield et al., 2020) or overprinted by  
103 strong scattering at shorter periods (van Driel et al., 2021; Karakostas et al., 2021). We  
104 correct for the presence of scattered waves in the seismic coda by examining frequency  
105 dependent polarization attributes (FDPAs) (e.g., Park et al., 1987). Here, we use the S-  
106 transform (Stockwell et al., 1996) of the three-component waveforms and calculate a 3  
107 x 3 cross-component covariance matrix at each frequency in 80% overlapping time win-  
108 dows whose duration is inversely proportional to frequency. The relative sizes of the eigen-  
109 values of this covariance matrix are related to the degree of polarization of the particle  
110 motion, while the complex-valued components of the eigenvectors describe the particle  
111 motion ellipsoid in each time-frequency window. To search for Rayleigh waves, we com-  
112 bine FDPAs to highlight seismic arrivals with elliptically-polarized particle motion pre-  
113 dominantly in the vertical plane (Kim, Banerdt, et al., 2022). To further enhance the  
114 signal-to-noise ratio of our data, we shift a 200-s window across travel time predictions  
115 of the R2-R7 signals and perform a N-th root stacking (N=4) and assume that waves  
116 propagate along the great circle path (GCP), a commonly-made assumption in surface  
117 wave analysis on Earth (e.g., Moulik et al., 2022). We consider a range of GCPs based  
118 on the back azimuth uncertainties of the direct P-, S-waves, and minor-arc surface waves  
119 (Kawamura et al., 2022; Panning et al., 2023; Kim, Stähler, et al., 2022). Prediction win-  
120 dows for Rayleigh wave travel times are computed according to the depth sensitivity for  
121 each period range and the KKS21 model. The minor-arc Rayleigh wave (R1) is not in-  
122 cluded in the analysis to avoid producing a bias towards the minor-arc path. Here, we  
123 use a Hilbert envelope rather than the waveform to prevent distortion of seismic signals  
124 produced by nonlinear processing (e.g., Rost & Thomas, 2002).

125 Previously, little deviation for R1-R3 travel times in S1222a between the GCP and  
 126 the ray theoretical path has been reported for existing crustal thickness models of Mars  
 127 (Kim, Stähler, et al., 2022). To account for more realistic volumetric sensitivities for higher-  
 128 orbit Rayleigh wave propagation, we carry out a 3-D wavefield simulation using the spectral-  
 129 element method by Afanasiev et al. (2019). For our input model, we employ the 3-D crustal  
 130 velocity modeling scheme used in the analysis of 3-D ray tracing by Kim, Stähler, et al.  
 131 (2022). We produce a global crustal thickness map fixing the crustal thickness to 45 km  
 132 at the InSight location using the gravimetric method by Wieczorek et al. (2022). The  
 133 map used in this study has the crustal thickness ranges from 20 km to 90 km, the thinnest  
 134 in Hellas and the thickest in the Tharsis province with an average thickness of 53 km (Fig. 1B).  
 135 The initial crustal velocity profile is characterized by a positive velocity gradient of 0.02  
 136 km/s per km with an average shear velocity ( $V_S$ ) of 3.2 km/s based on previous sur-  
 137 face wave analyses of S1222a and the two large impacts, S1094b and S1000a (Fig. 1A).  
 138 We assume a  $V_P/V_S$  ratio of 1.81 from the free-surface transform analysis in Kim, Lekić,  
 139 et al. (2021). The 4-th order spectral-element mesh is constructed to globally resolve pe-  
 140 riods of 15 s at one element per wavelength, resulting in a total of 2.24 M elements. Vari-  
 141 ations in crustal thickness are modeled by deforming the outer layer of the unstructured  
 142 mesh to align with surface and Moho topography. Within the crustal layer, the veloc-  
 143 ity profile is extrapolated and vertically scaled based on the distribution of crustal thick-  
 144 ness range (e.g., Fig. 1B). For the mantle, we consider: (a) the 1-D reference velocity model  
 145 of KKS21 (solid, Fig. 1A) and (b) the recently updated 1-D models that have a 5% faster  
 146 uppermost mantle velocity resulting from a reduced mantle FeO content (hereafter Du-  
 147 ran2022; dashed, Fig. 1A).

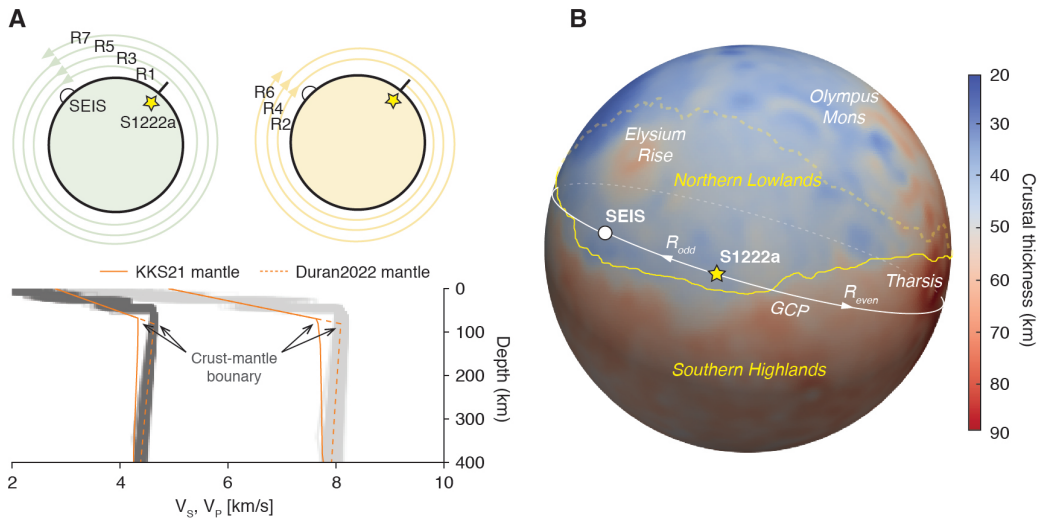


**Figure 1.** (A) Top diagram describes the direction of propagation and number of cycles for those surface waves orbiting around Mars in S1222a. Bottom shows 1-D interior models of Mars explored in this study. The crustal velocity profile constrained by previous surface wave studies are expanded to the existing mantle models of KKS21 (solid) and Duran2022 (dashed). For 3-D wavefield simulations, the two composite profiles are extrapolated by the thickness ranges shown in 1B. Gray profiles are the posterior distribution of models in Durán et al. (2022). (B) Crustal thickness distribution between the northern lowlands and southern highlands on Mars. S1222a and the lander locations are denoted by yellow and white symbols, respectively. Background colormap denotes the crustal thickness used for generating our 3-D crustal velocity model of Mars. Dichotomy boundary (yellow dashed) is based on Andrews-Hanna et al. (2008). SEIS = InSight seismometer; GCP = Great circle path

### 3 Result and Discussion

Our LP ( $\sim 30$  s) vertical-component envelope shows strong amplitude signals in the predicted time windows for R1, R2, and R3 traveling with an average group velocity range of 2.4-3.0 km/s (black curve, Fig. 2A). Weaker and more localized later-arrivals are observed within the predicted time windows for R4-R7. These arrivals appear to have relatively large elliptically-polarized energy in the vertical plane in the same period range (dashed brown, Fig. 2A). Linearly-polarized signals such as a small amplitude glitch (gray, Fig. 2A) or other body wave arrivals would show a negative correlation between envelope amplitude and the FDPA for Rayleigh waves. Arrivals outside the predicted windows may be associated with multipathing of the propagated surface waves in 3-D crustal structure or body-to-surface wave conversion. Whichever the case, these arrivals may have been contaminated by strong atmospheric noise as indicated by the lander modes (Dahmen et al., 2021) clearly visible during the 10-hour recording period (Fig. S1). For VLP ( $\sim 85$  s), the envelope amplitude and the corresponding FDPA curve is highly correlated and both data show distinctive peaks observed up to the R6 window with a higher traveling speed of 3.6-4.0 km/s (Fig. 2B). Notably, the peak shown in the R3 window has the smallest amplitude and polarization across the peaks associated with R1-R6. The observed peak in the R7 window has a relatively large amplitude but is weakly polarized.

Averaging across the R2-R7 signals, we observe the strongest amplitude signals at 30 s and 85 s central periods, propagating with distinctively different group velocities of 2.9 km/s and 3.8 km/s, respectively, in both amplitude and polarization stacks (Fig. 2C-D). At 30 s, similar group velocities have been independently reported by other studies for the R2 and R3 arrivals in S1222a (Kim, Stähler, et al., 2022; Li et al., 2022; Panning et al., 2023). Unlike typical, smoothly-varying surface wave dispersion curves, as predicted by the existing 1-D models (e.g., Durán et al., 2022; Drilleau et al., 2022) (Fig. S2), the observed group velocities show an apparent jump at intermediate periods between 20 s and 100 s and do not appear to constructively interfere across multiple orbits of Mars (Fig. S3). Such abruptness in dispersion and the observed low and high velocities from the R2-R7 signals cannot be solely attributed by elliptically-polarized martian wind (e.g., Stutzmann et al., 2021) contaminating the data which is unlikely to be recorded with the apparent periodicity for both LP and VLP data. At much longer period between 100-200 s, a similar group velocity close to 3.8 km/s for the excitation of R2 has been reported by using ambient noise correlations (Deng & Levander, 2022). A normal mode study on Mars has also shown some potential excitation of the fundamental mode surface waves in comparable period ranges between 120-300 s (Lognonné et al., under review).

The predicted dispersion curves using a suite of 1-D models with varying crustal thickness illustrate that the two end-member group velocities at LP and VLP appear as a type of stationary phase or “Airy-phase” (Aki & Richards, 2002) across different periods (Fig. S4). Depending on crustal thickness in a model, however, the rise and fall of the velocities at intermediate periods will vary substantially and would not constructively interfere across multiple orbits of Mars. Such Airy-phase is often associated with the amplification of Rayleigh waves on Earth that can propagate for considerable distances across the continental crust (Ewing & Press, 1956) and mantle (Ewing & Press, 1954). The observation of Rayleigh waves traveling over multiple orbits on the seismic recording of a relatively small-magnitude quake ( $M_W^{ma}$  4.6) suggests those stationary values of group velocities on Mars could be occurring close to 30 s and 85 s central periods.

Our 3-D wavefield simulations also show that large-scale variations in crustal thickness across the equatorial dichotomy are necessary to reproduce this behavior (Fig. S5-S6). Using our 3-D model, we find the spectra of the R2-R7 arrivals in synthetic waveform is largely discontinuous in time and frequency. This feature becomes more evident for Rayleigh waves propagating in higher-orbits beyond R3. The variation in amplitude

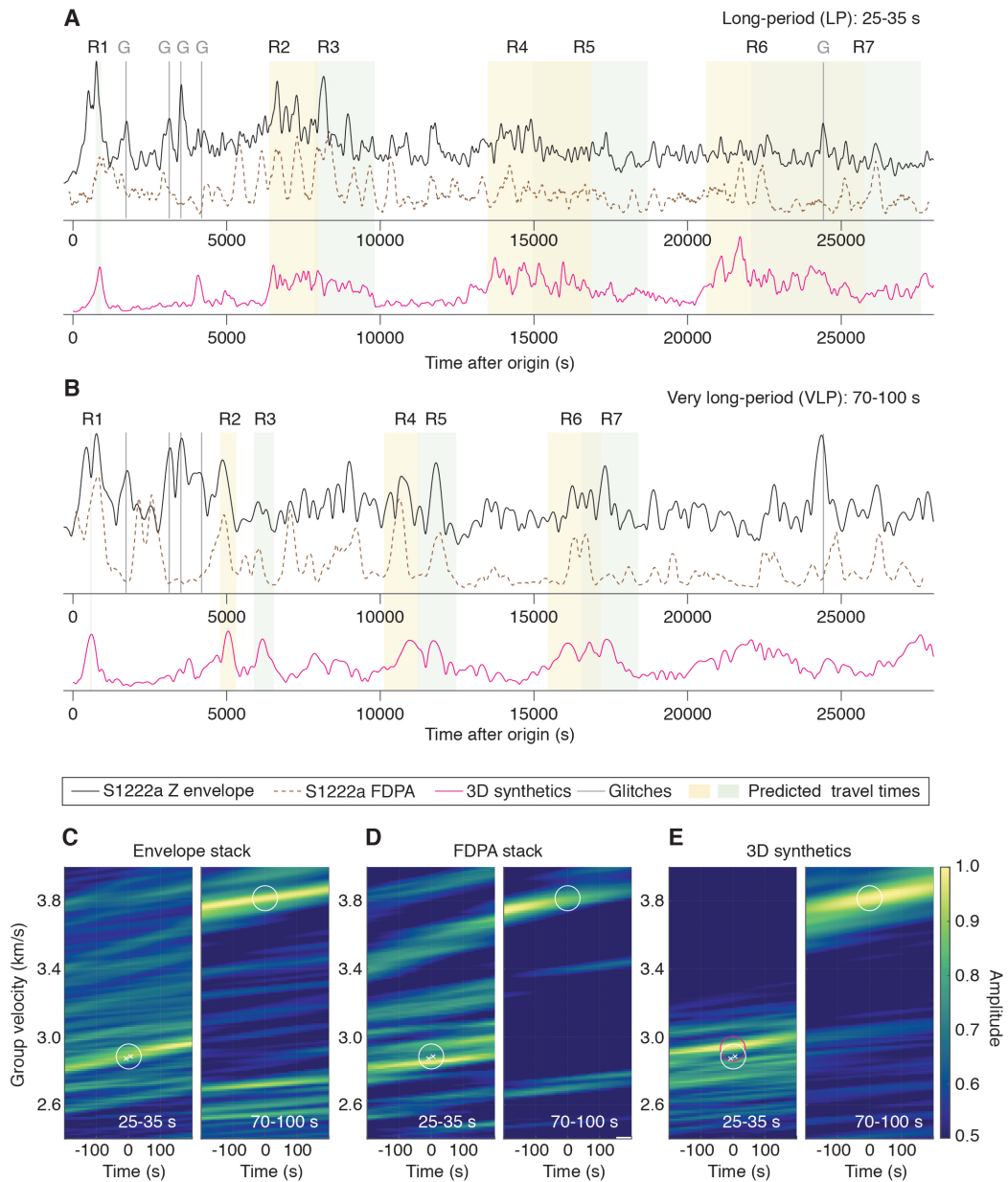


**Figure 2.** Vertical-component envelopes of the S1222a deglitched waveform (black) and FDPA (dashed brown) filtered between (A) 25-35 s (LP) and (B) 70-100 s periods (VLP). Shaded areas indicate the predicted time windows of R1-R7 arrivals base on the group velocities ranging from 2.4-3.0 km/s to 3.6-4.0 km/s for LP and VLP data, respectively. Glitches are shown by gray lines. Envelopes in magenta are based on a 3-D wavefield simulation using the model with crustal thickness variation shown in Fig. 1. Group velocity measurements of R2-R7 (white and magenta circles) are obtained by Nth-root stacking of the time-series in (A-B) for (C-D) data and (E) synthetics. White crosses are from independent analyses of R2 and R3 by Kim, Stähler, et al. (2022). See Fig. S3 for the complete analysis between 25-100 s with narrow-band filters. G = glitches; FDPA = frequency dependent polarization attribute

of surface waves propagating toward the minor-arc vs. major-arc directions (i.e.,  $R_{\text{odd}}$  vs.  $R_{\text{even}}$ ) also supports the evidence for lateral variation in crustal structure, likely due to (de)focusing of those waves (e.g., Romanowicz, 1987). Therefore, our observation of the absence of dispersion between  $\sim 30$ -85 s for R2-R7 in S1222a and their associated amplitude change substantiate the choice of our 3-D model with large variation in crustal thickness (i.e., 20-90 km)(Fig. 1B) as these observations cannot be explained by existing 1-D models assuming a constant crustal thickness (Fig. S2).

The group velocity obtained for the largest amplitudes seen in the synthetic LP stack is consistent with our R2-R7 measurement of  $\sim 2.9$  km/s (with a small uncertainty of  $<2\%$ ; c.f., white and magenta symbols)(Fig. 2E), indicating that the average speed at which R2-R7 travel within the crust can be well-recovered with our 3-D model even with a large variation in crustal thickness (e.g., Fig. 1B). For the synthetic VLP stack, we find that the observed group velocity is strongly dependent on the versions of 1-D mantle models implemented in our analysis since the sensitivity of 70-100 s Rayleigh waves on Mars is predominantly between 75-115 km, a depth range in the uppermost mantle (Fig. S7). For example, the recent 1-D models produced by Durán et al. (2022) or Drilleau et al. (2022) have a 5% faster uppermost mantle than KKS21 (Fig. 1A). Our R2-R7 measurements are better fits to the newer sets of models that are based on a lower mantle FeO content compared to the KKS21 model that uses Wänke-Dreibus or Taylor compositions (Wänke et al., 1994; Taylor, 2013)(c.f., Fig. 2E and Fig. S8). This difference in seismic wavespeeds in existing models of the uppermost mantle, however, does not significantly affect body wave travel times with limited sensitivity and geographical coverage nor the estimated event locations (Fig. 3). Therefore, the new observations of R2-R7 provide a promising means of refining the 1-D models of the planet’s radially symmetric structure, verifying the major element distribution of the martian mantle and determining the crustal thickness variations.

To find the average crustal thickness along the GCP from S1222a to the InSight lander, we carry out a systematic model-space search seeking average crustal  $V_S$ , thickness, and uppermost mantle  $V_S$  that fit the observed velocities of R2-R7 (Fig. 4A). We obtain a distribution of allowable velocities and thicknesses, with mean  $V_S$  of 3.38 km/s and 4.41 km/s for crustal and uppermost mantle, respectively, and a mean crustal thickness of 50 km beneath the GCP with an interquartile range between 44 and 58 km (magenta, Fig. 4A). This estimate of GCP-averaged crustal thickness and its uncertainty can be used as a robust anchoring-point and extrapolated globally using the existing models of crustal thickness based on gravimetric modeling (Wieczorek et al., 2022), which on their own suffer from a trade-off between average crustal density and thickness.

Crustal thickness directly beneath the lander based on RF analyses (Knapmeyer-Endrun et al., 2021; Kim, Lekić, et al., 2021) has previously been used as an anchoring-point to yield estimates of the average crustal thickness on Mars in the 30-72 km range. Here, we produce various crustal thickness models following the gravimetric modeling steps described in Wieczorek et al. (2022)(Fig. 4B). As an anchoring-point beneath the lander, we use the thickness of a three-layered crust ranging from 31 km to 47 km based on the previous RF analyses. Two end-member dichotomy structures with a uniform crustal density ranging from 2550 kg/m<sup>3</sup> to 3050 kg/m<sup>3</sup> (diamond symbol, Fig. 4B) and a model with a density contrast between 100-500 kg/m<sup>3</sup> across the dichotomy boundary have been tested (circle symbol, Fig. 4B). For the mantle and core beneath the lithosphere, we consider four plausible 1-D density profiles including both pre- and post-mission publications in Taylor (2013); Yoshizaki and McDonough (2020); Stähler et al. (2021); Khan et al. (2022).

Using the interquartile range of crustal thickness distribution along the GCP constrained by the R2-R7 analysis (magenta lines, Fig. 4A) against those from all models considered above, we were able to improve estimates of the average crustal thickness by ruling out the majority of those crustal models that have a  $>200$  kg/m<sup>3</sup> density contrast

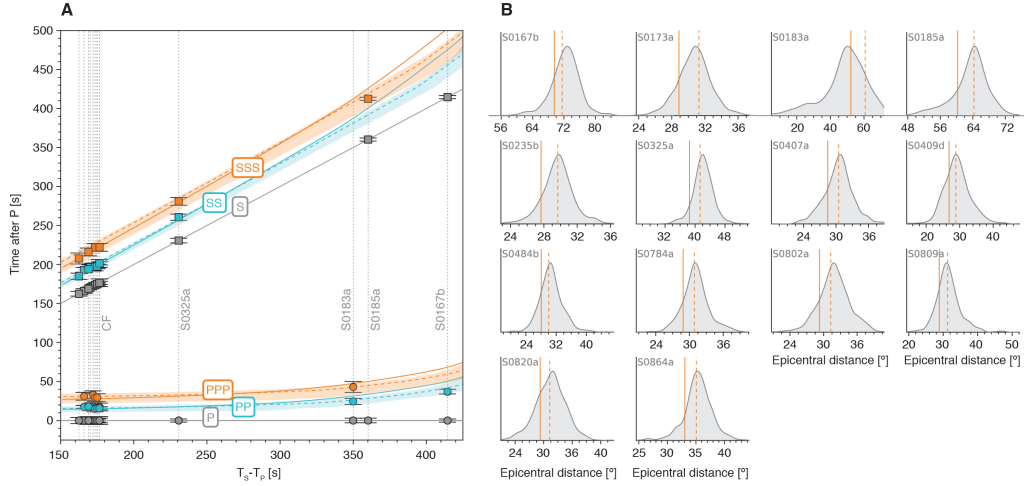


**Figure 3.** (A) Differential travel-time plot for available body wave measurements from quality A, B and C events and prediction by the inverted models of Durán et al. (2022)(shaded). Prediction by the composite models (Fig. 1B) with the mantle structure of KKS21 and the composite model with Duran2022 are shown by solid and dashed lines, respectively. Events are aligned by their observed S-P travel time difference. Farside events (S0976a and S1000a; Horleston et al., 2022) are excluded since, besides the phases that allow for their alignment, no body-waves exclusive to the upper mantle and crustal structure were identified. CF = Cerberus Fossae event cluster. Note that the surface-reflected S-wave arrival (SS or SSS) of S0167b, categorized as a quality C event by the Marsquake Service (Clinton et al., 2021), was removed due to the lack of consensus on its nature (see Khan et al., 2021; Durán et al., 2022). (B) Distribution of the event distances from the inverted models in (Durán et al., 2022) (gray). Solid and dashed lines indicate the corresponding epicentral distances for the composite models (Fig. 1B) by fitting the predicted S-P travel times.

254 across the dichotomy (Fig. 4B). As a result, we obtain an estimate of the global average  
 255 crustal thickness range between 42-56 km from the remaining models (symbols in  
 256 magenta, Fig. 4B), which is a significantly narrower range than previously available. This  
 257 implies large differences in crustal thickness between the northern lowlands and the south-  
 258 ern highlands (up to  $\sim 30$  km), and places new constraints on the average global thick-  
 259 ness of the martian crust, evidently thicker than the terrestrial (Dziewonski & Ander-  
 260 son, 1981; Huang et al., 2013) and the lunar crusts (Wieczorek et al., 2013) (Fig. 4C).

261 Of the major rocky bodies in the inner solar system for which constraints are avail-  
 262 able, Mars very likely has the thickest crust (i.e., 42-56 km). Based largely on seismic  
 263 data, Earth’s crust averages only about 24 km in thickness. The thickness of the lunar  
 264 crust, which is anchored by Apollo seismic data, is in the range of 34-43 km (Wieczorek  
 265 et al., 2013)(Fig. 4C). For the other bodies, there are no seismic data and crustal thick-  
 266 ness constraints are based solely on gravity and topography measurements. Neverthe-  
 267 less, it is likely that on average, the thickness of the venusian crust is in the range of about  
 268 8-26 km (James et al., 2013; Maia & Wieczorek, 2022) and the mercurian crust in the  
 269 range of 17-53 km (Padovan et al., 2015) or possibly even thinner (15-37 km; Sori, 2018).  
 270 Even the crust of 4-Vesta may be broadly in this range with one estimate at 24 km (Ermakov  
 271 et al., 2014). Accordingly, variations in crustal thicknesses of these rocky bodies appear  
 272 to be within a factor of about 3-4 (McLennan, 2022). This is in contrast to planetary  
 273 crustal masses which vary by well over an order of magnitude relative to the size of their

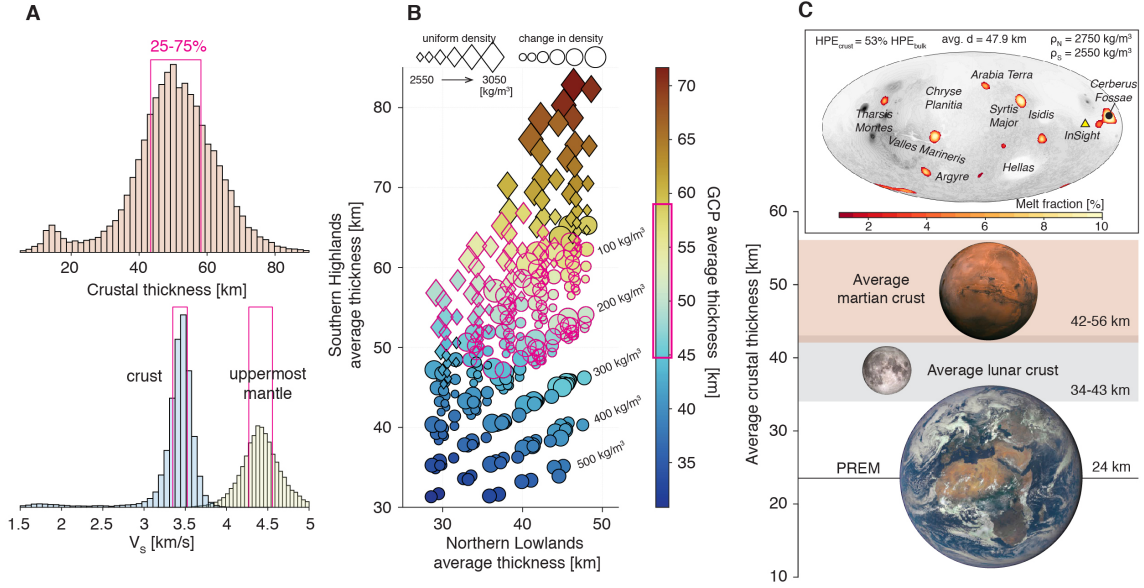


**Figure 4.** (A) Posterior distribution of the crustal and mantle  $V_s$  and crustal thickness along the GCP of S1222a. Interquartile range of the distribution is shown by red outlines. (B) Average crustal thickness of northern lowlands vs. southern highlands for global crustal thickness models with crustal densities ranging from 2550-3050  $\text{kg/m}^3$  with (circle symbol) and without a density contrast (diamond symbol) across the dichotomy. Dichotomy boundary is based on Andrews-Hanna et al. (2008). Colormap denotes the mean crustal thickness along the GCP for each model. Those models within the red outline are compatible with the posterior distribution in (A). (C) New global average crustal thickness range obtained by the model selection in (B) in comparison to that of the Earth and the Moon where constraints based on seismic data are available. Inset shows the best-fitting thermal evolution model of Plesa et al. (2018) computed with the new crustal constraint in (C). PREM = Preliminary Reference Earth Model. HPE = Heat-producing element

274 respective primitive mantles, between about 0.6% for Venus (and a similar value of 0.7%  
 275 for Earth; Huang et al., 2013) to as much as 9.5% for Mercury and 14% for 4-Vesta (McLennan,  
 276 2022). Our results are consistent with Mars being intermediate among these values with  
 277 the crust representing about 4-5% of the primitive mantle mass. Therefore, the degree  
 278 of silicate differentiation into planetary crusts is more a function of overall planetary size  
 279 than to crustal thickness and smaller bodies tend to have thicker crusts and increased  
 280 degrees of mantle processing to form those crusts (O'Rourke & Korenaga, 2012; McLennan,  
 281 2022).

282 The tighter constraints on the crustal thickness obtained here compared to previ-  
 283 ously derived values from the RF analysis (Knapmeyer-Endrun et al., 2021) provide im-  
 284 portant information for thermal evolution models of the interior of Mars (Plesa et al.,  
 285 2018, 2021; Khan et al., 2021; Knapmeyer-Endrun et al., 2021; Plesa et al., 2022). To-  
 286 gether, this can help to further refine the present-day temperature distribution and amount  
 287 of heat-producing elements within the crust. Thermal evolution models produced by us-  
 288 ing a maximum density contrast of  $<200 \text{ kg/m}^3$  across the dichotomy constrained by the  
 289 R2-R7 analysis show that more than half of the total heat production but less than 70%  
 290 of the total heat source budget needs to be in the crust, due to enrichment in the con-  
 291 centrations of Th, K, and U, in order to produce local melt zones in the mantle at present

day (see detailed results in Fig. S9-S10). This crustal heat production range is consistent with the study of Knapmeyer-Endrun et al. (2021). For three end-member crustal models tested in Fig. S9-S10, we obtained enrichment factors between 8.2-14.3 (corresponding to a crustal heat production of 46.7-64.4 pW/kg). These enrichment factors are close to, but extend to slightly larger values than the enrichment estimated from GRS data 8 - 10.3 (crustal heat production of 46-51 pW/kg; Hahn et al., 2011). Interestingly, our best-fitting model with a 200 kg/m<sup>3</sup> variable density favors mantle plumes that can produce melt up to the present day in and around Cerberus Fossae (inset, Fig. 4D), supporting the interpretation from gravity and topography data (Broquet & Andrews-Hanna, 2022) and from seismic observations (Stähler et al., 2022). Therefore, our study offers a promising opportunity for further evaluating the plume hypothesis beneath Cerberus Fossae.

#### 4 Open Research

The InSight event catalogue <https://doi.org/10.12686/a17> and waveform data are available from the IRIS-DMC <http://ds.iris.edu/ds/nodes/dmc/tools/mars-events/>, NASA-PDS <https://pds-geosciences.wustl.edu/missions/insight/seis.htm> and IGP data center [https://doi.org/10.18715/SEIS.INSIGHT.XB\\_2016](https://doi.org/10.18715/SEIS.INSIGHT.XB_2016).

#### Acknowledgments

This paper is InSight contribution number 315. The authors acknowledge the NASA, the CNES, their partner agencies and Institutions (UKSA, SSO, DLR, JPL, IGP-CNRS, ETHZ, IC, and MPS-MPG) and the flight operations team at JPL, SISMOC, MSDS, IRIS-DMC, and PDS for providing the SEED SEIS data. Marsquake Service (MQS) operations at ETH are supported by ETH Research grant ETH-06 17-02. ETH authors recognize support from the ETH+ funding scheme (ETH+02 19-1: “Planet Mars”). V.L. acknowledge funding from NASA grant 80NSSC18K1628 and NASA Solar System Exploration Research Virtual Institute (SSERVI) Cooperative Agreement 80NSSC19M0216. SMM acknowledges funding from NASA grant 80NSSC18K1622.

#### References

- Afanasiev, M., Boehm, C., van Driel, M., Krischer, L., Rietmann, M., May, D. A., ... Fichtner, A. (2019). Modular and flexible spectral-element waveform modelling in two and three dimensions. *Geophysical Journal International*, 216(3), 1675–1692.
- Aki, K., & Richards, P. G. (2002). *Quantitative seismology*.
- Andrews-Hanna, J. C., Zuber, M. T., & Banerdt, W. B. (2008). The borealis basin and the origin of the martian crustal dichotomy. *Nature*, 453(7199), 1212–1215.
- Banerdt, W. B., Smrekar, S. E., Banfield, D., Giardini, D., Golombek, M., Johnson, C. L., ... et al. (2020). Initial results from the insight mission on mars. *Nature Geoscience*, 13(3), 183–189.
- Banfield, D., Spiga, A., Newman, C., Forget, F., Lemmon, M., Lorenz, R., ... et al. (2020). The atmosphere of mars as observed by insight. *Nature Geoscience*, 13(3), 190–198.
- Beghein, C., Li, J., Weidner, E., Maguire, R., Wookey, J., Lekić, V., ... Banerdt, W. (2022). Crustal anisotropy in the martian lowlands from surface waves. *Geophysical Research Letters*, 49(24), e2022GL101508.
- Broquet, A., & Andrews-Hanna, J. C. (2022). Geophysical evidence for an active mantle plume underneath elysium planitia on mars. *Nature Astronomy*, 1–10.
- Ceylan, S., Clinton, J. F., Giardini, D., Stähler, S. C., Horleston, A., Kawamura, T., ... et al. (2022). The marsquake catalogue from insight, sols 0–1011. *Physics*

- 341 of the *Earth and Planetary Interiors*, 333, 106943.
- 342 Clinton, J. F., Ceylan, S., van Driel, M., Giardini, D., Stähler, S. C., Böse, M., ...  
 343 et al. (2021). The marsquake catalogue from insight, sols 0–478. *Physics of the*  
 344 *Earth and Planetary Interiors*, 310, 106595.
- 345 Dahmen, N. L., Zenhäusern, G., Clinton, J. F., Giardini, D., Stähler, S. C., Ceylan,  
 346 S., ... Banerdt, W. B. (2021, 10). Resonances and Lander Modes Observed  
 347 by InSight on Mars (1–9 Hz). *Bulletin of the Seismological Society of America*,  
 348 111(6), 2924–2950. doi: 10.1785/0120210056
- 349 Deng, S., & Levander, A. (2022). Autocorrelation  $r_2$  on mars. *Geophysical Research*  
 350 *Letters*, 49(17), e2022GL099580.
- 351 Drilleau, M., Samuel, H., Garcia, R. F., Rivoldini, A., Perrin, C., Michaut, C., ... et  
 352 al. (2022). Marsquake locations and 1-d seismic models for mars from insight  
 353 data. *Journal of Geophysical Research: Planets*, 127(9), e2021JE007067.
- 354 Durán, C., Khan, A., Ceylan, S., Zenhäusern, G., Staehler, S., Clinton, J., & Gia-  
 355 rdini, D. (2022). Seismology on mars: An analysis of direct, reflected, and  
 356 converted seismic body waves with implications for interior structure. *Physics*  
 357 *of the Earth and Planetary Interiors*, 325, 106851.
- 358 Dziewonski, A. M., & Anderson, D. L. (1981). Preliminary reference earth model.  
 359 *Physics of the earth and planetary interiors*, 25(4), 297–356.
- 360 Ermakov, A. I., Zuber, M. T., Smith, D. E., Raymond, C. A., Balmino, G., Fu,  
 361 R. R., & Ivanov, B. A. (2014). Constraints on vesta’s interior structure using  
 362 gravity and shape models from the dawn mission. *Icarus*, 240, 146–160.
- 363 Ewing, M., & Press, F. (1954). An investigation of mantle rayleigh waves. *Bulletin*  
 364 *of the Seismological Society of America*, 44(2A), 127–147.
- 365 Ewing, M., & Press, F. (1956). Rayleigh wave dispersion in the period range 10 to  
 366 500 seconds. *Eos, Transactions American Geophysical Union*, 37(2), 213–215.
- 367 Garcia, R. F., Daubar, I. J., Beucler, É., Posiolova, L. V., Collins, G. S., Lognonné,  
 368 P., ... et al. (2022). Newly formed craters on mars located using seismic and  
 369 acoustic wave data from insight. *Nature Geoscience*, 15(10), 774–780.
- 370 Giardini, D., Lognonné, P., Banerdt, W. B., Pike, W. T., Christensen, U., Cey-  
 371 lan, S., ... Yana, C. (2020). The Seismicity of Mars. *Nat. Geosci.* doi:  
 372 10.1038/s41561-020-0539-8
- 373 Hahn, B., McLennan, S., & Klein, E. (2011). Martian surface heat production and  
 374 crustal heat flow from Mars Odyssey Gamma-Ray spectrometry. *Geophysical*  
 375 *Research Letters*, 38(14).
- 376 Horleston, A. C., Clinton, J. F., Ceylan, S., Giardini, D., Charalambous, C., Irving,  
 377 J. C. E., ... Banerdt, W. B. (2022, 04). The Far Side of Mars: Two Dis-  
 378 tant Marsquakes Detected by InSight. *The Seismic Record*, 2(2), 88–99. doi:  
 379 10.1785/0320220007
- 380 Huang, Y., Chubakov, V., Mantovani, F., Rudnick, R. L., & McDonough, W. F.  
 381 (2013). A reference earth model for the heat-producing elements and as-  
 382 sociated geoneutrino flux. *Geochemistry, Geophysics, Geosystems*, 14(6),  
 383 2003–2029.
- 384 InSight Marsquake Service. (2022). *Mars Seismic Catalogue, InSight Mission;*  
 385 *V3 2020-07-01. ETHZ, IPGP, JPL, ICL, ISAE-Supaero, MPS, Univ Bristol.*  
 386 *Dataset.* doi: <https://doi.org/10.12686/a19>
- 387 InSight Marsquake Service. (2023). *Mars seismic catalogue, insight mission; v13*  
 388 *2023-01-01.* ETHZ, IPGP, JPL, ICL, Univ. Bristol. Retrieved from [https://](https://www.insight.ethz.ch/seismicity/catalog/v13)  
 389 [www.insight.ethz.ch/seismicity/catalog/v13](https://www.insight.ethz.ch/seismicity/catalog/v13) doi: 10.12686/a19
- 390 Irving, J., Antonangeli, D., Banerdt, B., Li, J., Bozdog, E., Stähler, S., ... Stutz-  
 391 mann, E. (2022, 01). First observations of seismic waves travelling through the  
 392 martian core..
- 393 James, P. B., Zuber, M. T., & Phillips, R. J. (2013). Crustal thickness and support  
 394 of topography on venus. *Journal of Geophysical Research: Planets*, 118(4),  
 395 859–875.

- 396 Karakostas, F., Schmerr, N., Maguire, R., Huang, Q., Kim, D., Lekic, V., ... oth-  
 397 ers (2021). Scattering attenuation of the martian interior through coda-wave  
 398 analysis. *Bulletin of the Seismological Society of America*, *111*(6), 3035–3054.
- 399 Kawamura, T., Clinton, J. F., Zenhäusern, G., Ceylan, S., Horleston, A. C., Dah-  
 400 men, N. L., ... Banerdt, W. B. (2022). S1222a - the largest marsquake  
 401 detected by insight. *Geophysical Research Letters*, e2022GL101543. doi:  
 402 <https://doi.org/10.1029/2022GL101543>
- 403 Khan, A., Ceylan, S., van Driel, M., Giardini, D., Lognonné, P., Samuel, H., ... et  
 404 al. (2021). Upper mantle structure of mars from insight seismic data. *Science*,  
 405 *373*(6553), 434–438.
- 406 Khan, A., Sossi, P. A., Liebske, C., Rivoldini, A., & Giardini, D. (2022). Geophys-  
 407 ical and cosmochemical evidence for a volatile-rich mars. *Earth and Planetary*  
 408 *Science Letters*, *578*, 117330.
- 409 Kim, D., Banerdt, W., Ceylan, S., Giardini, D., Lekić, V., Lognonné, P., ... et al.  
 410 (2022). Surface waves and crustal structure on mars. *Science*, *378*(6618),  
 411 417–421.
- 412 Kim, D., Davis, P., Lekić, V., Maguire, R., Compaire, N., Schimmel, M., ... et al.  
 413 (2021). Potential pitfalls in the analysis and structural interpretation of seis-  
 414 mic data from the mars insight mission. *Bulletin of the Seismological Society*  
 415 *of America*, *111*(6), 2982–3002.
- 416 Kim, D., Lekić, V., Irving, J. C., Schmerr, N., Knapmeyer-Endrun, B., Joshi, R., ...  
 417 et al. (2021). Improving constraints on planetary interiors with pps receiver  
 418 functions. *Journal of Geophysical Research: Planets*, *126*(11), e2021JE006983.
- 419 Kim, D., Stähler, S., Ceylan, S., Lekic, V., Maguire, R., Zenhäusern, G., ... et al.  
 420 (2022). Structure along the martian dichotomy constrained by rayleigh and  
 421 love waves and their overtones. *Geophysical Research Letters*, e2022GL101666.
- 422 Knapmeyer-Endrun, B., Panning, M. P., Bissig, F., Joshi, R., Khan, A., Kim, D., ...  
 423 et al. (2021). Thickness and structure of the martian crust from insight seismic  
 424 data. *Science*, *373*(6553), 438–443.
- 425 Li, J., Beghein, C., Lognonné, P., McLennan, S. M., Wiczorek, M., Panning, M., ...  
 426 Banerdt, W. B. (2022). Different martian crustal seismic velocities across the  
 427 dichotomy boundary from multi-orbiting surface waves. *Geophysical Research*  
 428 *Letters*, e2022GL101243.
- 429 Lognonné, P., Banerdt, W. B., Giardini, D., Pike, W. T., Christensen, U., Laudet,  
 430 P., ... et al. (2019). Seis: Insight’s seismic experiment for internal structure of  
 431 mars. *Space Science Reviews*, *215*, 1–170.
- 432 Lognonné, P., Schimmel, M., Stutzmann, E., Davis, P., Drilleau, M., Sainton, G., ...  
 433 Panning, B. W. B., M. P. (under review). Detection of mars normal modes  
 434 from s1222 event and seismic noise. *Geophysical Research Letters*.
- 435 Lognonné, P., Banerdt, W., Pike, W., Giardini, D., Christensen, U., Garcia, R.,  
 436 ... Zweifel, P. (2020). Constraints on the shallow elastic and anelas-  
 437 tic structure of Mars from InSight seismic data. *Nat. Geosci.* doi:  
 438 10.1038/s41561-020-0536-y
- 439 Maia, J. S., & Wiczorek, M. A. (2022). Lithospheric structure of venusian crustal  
 440 plateaus. *Journal of Geophysical Research: Planets*, *127*(2), e2021JE007004.
- 441 McLennan, S. M. (2022). Composition of planetary crusts and planetary differentia-  
 442 tion. In *Planetary volcanism across the solar system* (pp. 287–331). Elsevier.
- 443 Moulik, P., Lekic, V., Romanowicz, B., Ma, Z., Schaeffer, A., Ho, T., ... others  
 444 (2022). Global reference seismological data sets: multimode surface wave  
 445 dispersion. *Geophysical Journal International*, *228*(3), 1808–1849.
- 446 O’Rourke, J. G., & Korenaga, J. (2012). Terrestrial planet evolution in the stagnant-  
 447 lid regime: Size effects and the formation of self-destabilizing crust. *Icarus*,  
 448 *221*(2), 1043–1060.
- 449 Padovan, S., Wiczorek, M. A., Margot, J.-L., Tosi, N., & Solomon, S. C. (2015).  
 450 Thickness of the crust of mercury from geoid-to-topography ratios. *Geophysical*

- 451 *Research Letters*, 42(4), 1029–1038.
- 452 Panning, M. P., Banerdt, W. B., Beghein, C., Carrasco, S., Ceylan, S., Clinton,  
453 J. F., ... Zenhäusern, G. (2023). Locating the largest event observed on  
454 mars with multi-orbit surface waves. *Geophysical Research Letters*, 50(1),  
455 e2022GL101270. doi: <https://doi.org/10.1029/2022GL101270>
- 456 Park, J., Vernon III, F. L., & Lindberg, C. R. (1987). Frequency dependent polariza-  
457 tion analysis of high-frequency seismograms. *Journal of Geophysical Research:*  
458 *Solid Earth*, 92(B12), 12664–12674.
- 459 Plesa, A.-C., Bozdağ, E., Rivoldini, A., Knapmeyer, M., McLennan, S. M., Padovan,  
460 S., ... Spohn, T. (2021). Seismic velocity variations in a 3d martian mantle:  
461 Implications for the insight measurements. *Journal of Geophysical Research:*  
462 *Planets*, 126(6), e2020JE006755. doi: <https://doi.org/10.1029/2020JE006755>
- 463 Plesa, A.-C., Padovan, S., Tosi, N., Breuer, D., Grott, M., Wieczorek, M., ...  
464 Banerdt, W. (2018). The thermal state and interior structure of Mars. *Geo-*  
465 *physical Research Letters*, 45(22), 12–198.
- 466 Plesa, A.-C., Wieczorek, M., Knapmeyer, M., Rivoldini, A., Walterova, M., &  
467 Breuer, D. (2022). Interior dynamics and thermal evolution of mars—a geody-  
468 namic perspective. *Geophysical Exploration of the Solar System*, 63, 179–230.
- 469 Posiolova, L. V., Lognonné, P., Banerdt, W. B., Clinton, J., Collins, G. S., Kawa-  
470 mura, T., ... Zenhäusern, G. (2022). Largest recent impact craters on mars:  
471 Orbital imaging and surface seismic co-investigation. *Science*, 378(6618),  
472 412–417. doi: [10.1126/science.abq7704](https://doi.org/10.1126/science.abq7704)
- 473 Romanowicz, B. (1987). Multiplet-multiplet coupling due to lateral heterogene-  
474 ity: asymptotic effects on the amplitude and frequency of the earth’s normal  
475 modes. *Geophysical Journal International*, 90(1), 75–100.
- 476 Rost, S., & Thomas, C. (2002). Array seismology: Methods and applications. *Re-*  
477 *views of geophysics*, 40(3), 2–1.
- 478 Scholz, J.-R., Widmer-Schmidrig, R., Davis, P., Lognonné, P., Pinot, B., Garcia,  
479 R. F., ... Banerdt, W. B. (2020). Detection, analysis, and removal of  
480 glitches from insight’s seismic data from mars. *Earth and Space Science*,  
481 7(11), e2020EA001317. doi: <https://doi.org/10.1029/2020EA001317>
- 482 Sori, M. M. (2018). A thin, dense crust for mercury. *Earth and Planetary Science*  
483 *Letters*, 489, 92–99.
- 484 Stähler, S. C., Khan, A., Banerdt, W. B., Lognonné, P., Giardini, D., Ceylan, S.,  
485 ... et al. (2021). Seismic detection of the martian core. *Science*, 373(6553),  
486 443–448.
- 487 Stähler, S. C., Mittelholz, A., Perrin, C., Kawamura, T., Kim, D., Knapmeyer, M.,  
488 ... et al. (2022). Tectonics of cerberus fossae unveiled by marsquakes. *Nature*  
489 *Astronomy*, 1–11.
- 490 Stockwell, R. G., Mansinha, L., & Lowe, R. (1996). Localization of the complex  
491 spectrum: the s transform. *IEEE transactions on signal processing*, 44(4),  
492 998–1001.
- 493 Stutzmann, E., Schimmel, M., Lognonné, P., Horleston, A., Ceylan, S., van Driel,  
494 M., ... Spiga, A. (2021). The polarization of ambient noise on mars.  
495 *Journal of Geophysical Research: Planets*, 126(1), e2020JE006545. doi:  
496 <https://doi.org/10.1029/2020JE006545>
- 497 Taylor, G. J. (2013). The bulk composition of mars. *Geochemistry*, 73(4), 401–420.
- 498 van Driel, M., Ceylan, S., Clinton, J. F., Giardini, D., Horleston, A., Margerin, L.,  
499 ... others (2021). High-frequency seismic events on mars observed by insight.  
500 *Journal of Geophysical Research: Planets*, 126(2), e2020JE006670.
- 501 Wieczorek, M. A., Broquet, A., McLennan, S. M., Rivoldini, A., Golombek, M., An-  
502 tonangeli, D., ... Banerdt, W. B. (2022). Insight constraints on the global  
503 character of the martian crust. *Journal of Geophysical Research: Planets*,  
504 127(5), e2022JE007298. doi: <https://doi.org/10.1029/2022JE007298>
- 505 Wieczorek, M. A., Neumann, G. A., Nimmo, F., Kiefer, W. S., Taylor, G. J.,

- 506 Melosh, H. J., ... Zuber, M. T. (2013). The crust of the moon as seen by  
507 grail. *Science*, *339*(6120), 671-675. doi: 10.1126/science.1231530
- 508 Wänke, H., Dreibus, G., Wright, I. P., Cowley, S. W. H., Runcorn, S. K., & South-  
509 wood, D. J. (1994). Chemistry and accretion history of mars. *Philosophical*  
510 *Transactions of the Royal Society of London. Series A: Physical and Engineer-*  
511 *ing Sciences*, *349*(1690), 285-293. doi: 10.1098/rsta.1994.0132
- 512 Yoshizaki, T., & McDonough, W. F. (2020). The composition of mars. *Geochimica*  
513 *et Cosmochimica Acta*, *273*, 137-162.